

Measurements of wave velocity and electrical conductivity of an amphibolite from southwestern margin of the Tarim Basin at pressures to 1.0 GPa and temperatures to 700 °C: comparison with field observations

Wenge Zhou, Dawei Fan, Yonggang Liu and Hongsen Xie

Laboratory of the Earth's Interior and Geofluid, Institute of Geochemistry, Chinese Academy of Science, Guiyang, Guizhou 550002, China. E-mail: zhouwenge@vip.gyig.ac.cn

Accepted 2011 September 5. Received 2011 July 6; in original form 2009 September 7

SUMMARY

In situ measurements of elastic wave velocities and electrical conductivities in the three structural directions (normal to foliation Z , perpendicular to lineation in foliation Y and parallel to lineation X) for an amphibolite collected from southwestern margin of the Tarim Basin, north-west China, were carried out in the laboratory. The elastic wave velocity was measured with the combined transmission–reflection method at pressures up to 1.0 GPa (at room temperature) and temperatures up to 700 °C (at 1.0 GPa) and the electrical conductivity was measured with the impedance spectroscopy from 250 to 700 °C at 1.0 GPa. The experimentally determined data included compressional (V_p) and shear wave velocities (V_s), velocity anisotropy (A_v), intrinsic pressure and temperature derivatives of V_p and V_s , electrical conductivity (σ), electrical conductivity anisotropy (A_σ) and the parameters of the Arrhenius relationship. Elastic wave velocities increase in the structural directions Z , Y , X , with V_p of 6.63, 6.78 and 6.95 km s⁻¹ and V_s of 3.75, 3.82 and 3.96 km s⁻¹ for Z , Y and X , respectively, at pressure of 1.0 GPa. Elastic wave velocities increase linearly with pressure at room temperature and pressures between 0.25 and 1.0 GPa and decrease linearly with increasing temperature at 1.0 GPa. The pressure coefficients of the sample are in the range of 0.1883–0.2308 km s⁻¹ GPa⁻¹ for V_p and 0.1149–0.1678 km s⁻¹ GPa⁻¹ for V_s . The temperature coefficients are in the range of 2.09–2.35 × 10⁻⁴ km s⁻¹ GPa⁻¹ for V_p and 1.28–1.68 × 10⁻⁴ km s⁻¹ GPa⁻¹ for V_s . The electrical conductivity increases with increasing temperature, consistent with the Arrhenius relationship. Activation energies for the three structural directions of the amphibolite are in the range of 0.71–0.75 eV. The amphibolite shows velocity anisotropy (4.15–4.86 per cent for V_p and 5.29–5.84 per cent for V_s at 0.25–1.0 GPa) and electrical conductivity anisotropy (11.1–25.2 per cent). Based on the regional crust model and geothermal gradient, velocity and electrical conductivity–depth profiles were calculated for the sample. These profiles were then compared with those derived from seismic reflection/refraction data and from electromagnetic data. Our results showed that the amphibolite sample has V_p and V_s in agreement with those of the middle and lower crust obtained from seismic reflection/refraction data, and σ in accord with that of the lower crust deduced from electromagnetic data. The lower crust of the electromagnetic crust model is roughly equivalent to the middle and lower crust layers of the seismic crust model. Therefore, it is suggested that the amphibolite may be one of the constituents of the present middle and lower crust in the Tarim Basin.

Key words: Electrical properties; High pressure behaviour; Acoustic properties.

1 INTRODUCTION

In situ laboratory measurements of elastic wave velocity and electrical conductivity of the crust rocks at high pressure and high temperature in combination with velocity- and conductivity-depth

profiles of the crust derived from geophysical investigation provide important constraints on the composition and deep structure of the crust (Frost *et al.* 1989; Christensen and Mooney 1995; Christensen 1996; Kern *et al.* 1996, 1999; Behn & Kelemen 2003; Freund 2003; Fuji-ta *et al.* 2004, 2007; Wang *et al.* 2005a,b). Over the past several

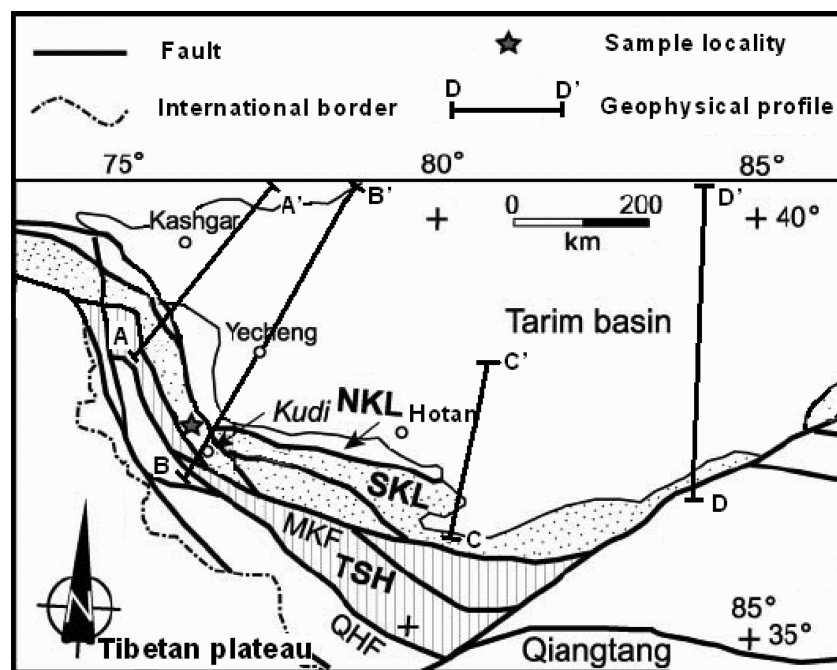


Figure 1. Schematic geological map of the southwestern margin of the Tarim Basin and adjacent regions (modified after Shao *et al.* 1997; Li *et al.* 2001; Xiao *et al.* 2002; Zhang *et al.* 2002). NKL, North Kunlun terrane; SKL, South Kunlun terrane; TSH, Tianshuihai terrane; MKF, Mazar–Kangxiwar fault; QHF, Qiertianshan–Hongshanhu fault.

decades, both elastic wave velocities and electrical conductivities for a variety of rocks have been investigated at high pressure and high temperature extensively (Birch 1960; Simmons 1964; Christensen 1965, 1966, 1995; Kern & Richter 1981; Ji *et al.* 1993; Ito & Tatsuiri 1995; Kariya & Shankland 1983; Shankland & Ander 1983; Glover & Vine 1992; Schilling *et al.* 1997; Partzsch *et al.* 2000; Freund 2003; Fuji-ta *et al.* 2004, 2007) to constrain the crust composition and structure (Christensen & Fountain 1975; Chroston & Evans 1983; Kern & Schenk 1988; Burke & Fountain 1990; Kern *et al.* 1993, 1996, 1999, 2009; Müller 1995; Rudnick & Fountain 1995; Gao *et al.* 1998; Zhao *et al.* 2001; Aizawa *et al.* 2002; Kitamura *et al.* 2003; Wang *et al.* 2005a,b). However, a combination of the elastic wave velocity with electrical conductivity to confine the composition and structure of the crust is rare (Schmeling 1985; Hyndman & Klempner 1989; Sato *et al.* 1989; Siegesmund *et al.* 1991). Furthermore, whether the crust composition model induced by the elastic wave velocity measured at high pressure and high temperature is consistent with that induced from the electrical conductivity is an open question.

In this study, we measured the elastic wave velocity and electrical conductivity for an amphibolite from southwestern margin of the Tarim Basin, northwest China, at 1.0 GPa and up to 700 °C. As a case study, we compared the experimental data with the field geophysical results, and confirmed that the composition model of crust deduced from the elastic wave velocity is consistent with that inferred from the electrical conductivity.

2 EXPERIMENTS

2.1 Geological setting and sample

The Tarim Basin is situated in northwest China. Its southwestern margin is a part of the Western Kunlun Orogen (WKO), which is located along the northern periphery of the Tibetan plateau (Fig. 1).

The WKO is generally interpreted as the result of the collision between the Tarim and Qiangtang blocks in Early Mesozoic time (Li & Xiao 1999), and is divisible into the North Kunlun, South Kunlun and Tianshuihai domains, separated by the Akaz and Mazar–Kangxiwar faults, respectively. The southwestern margin of the Tarim Basin includes the northwestern part of the North Kunlun and the South Kunlun domains. The North Kunlun domain represents the basement of the Tarim block, and the South Kunlun domain is mainly composed of the Buziwan (Kudi) ophiolite, the Yixieke arc, the Kudi gneiss and the Xianqiao arc (Xiao *et al.* 2002). Our sample was collected from the Kudi gneiss complex which is composed of hornblende/biotite gneisses and amphibolite (Fig. 1). The gneiss complex has been interpreted as a Proterozoic microcontinent derived from the Tarim block (Ding *et al.* 1996). The estimated peak metamorphic condition of the gneiss complex was 500–600 °C and 0.92–0.95 GPa (Ren & Gao 2002).

The experimental sample is an amphibolite. The amphibolite is massive, dark grey in colour, lacking secondary mineral alteration and fractures. It exhibits pronounced banding defined by plagioclase and amphibolite + biotite layers (Fig. 2a) and has a foliation and lineation defined by aligned amphibolite and biotite crystals. The foliation plane is parallel to the small-scale compositional banding. The sample is composed of amphibole (58.4 vol. per cent), plagioclase (32.3 vol. per cent), biotite (9.2 vol. per cent) and epidote + magnetite + sphene + apatite (<1.0 per cent), which is obtained by point counting analysis. The grain size of the amphibole, plagioclase and biotite is usually less than 0.6 mm. The grain size of the epidote, magnetite, sphene and apatite is less than 0.3 mm. The grains have the average aspect ratios of 1.6:1.3:1.0 for amphibole, 1.3:1.1:1.0 for plagioclase, 1.9:1.2:1.0 for biotite in the three structural directions. Major elements of the rock and minerals are presented in Table 1.

Two kinds of cylinder samples of the three structural directions, corresponding to normal to foliation Z, perpendicular to lineation

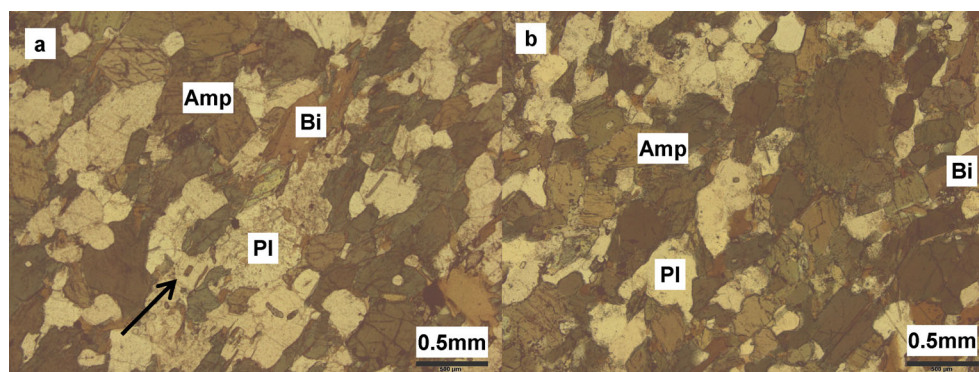


Figure 2. Micrographs of the sample perpendicular to the foliation before (a) and after (b) experiment in plane-polarized light. Foliation is defined by the alignment of amphibolite and biotite (indicated by the arrow in a). Amp, amphibole; Pl, plagioclase; Bi, biotite.

in foliation Y and parallel to lineation X , were prepared. One kind of cylinder sample with 6.0 mm in height and 10.0 mm in diameter was used for the elastic wave velocity measurement. The other with 4.0 mm in height and 6.0 mm in diameter was used for the electrical conductivity measurement. The cylinder samples were immersed in acetone for half an hour, and then cleaned in acetone by an ultrasonic cleaning instrument. The cleaned samples were wiped with filter paper. After dried in an oven at 50 °C for 3 h, the samples were stored in the same oven at 150 °C for more than 12 h. The temperature was increased at a very slow rate of 1 °C min⁻¹ from 50 to 150 °C to prevent the emergence of additional cracks.

2.2 Elastic wave velocity and electrical conductivity measurement

The experiments were performed in a multi-anvil pressure apparatus (YJ-3000t), at the Institute of Geochemistry, Chinese Academy of Sciences, Guiyang, China. The apparatus has been described by Xie *et al.* (1993) in detail. The pressure of the apparatus is calibrated with the melting curve of copper determined by the differential

thermal analysis method and from the quartz-coesite transition. The pressure is considered accurate to 1.5 per cent (Xie *et al.* 1993; Xue *et al.* 1994). The temperature is calibrated with a NiCr–NiSi thermocouple. The uncertainty in temperature measurement is less than ± 5 °C.

We measured the elastic wave velocities (V_p and V_s) of the amphibolite with the combined transmission–reflection method by using the 5077PR ultrasonic square wave pulsar/receiver unit (PANAMETRIC-NDT Incorporation, USA), TDS784A digital oscilloscope (Tektronix Corporation, USA) and LiNiO₃ transducer operating at 1 MHz for V_p and 2 MHz for V_s . Detailed descriptions of the ultrasonic system have been given by Liu *et al.* (2000, 2002). The combined transmission–reflection method is briefly presented here. For the elastic wave velocity of samples (Fig. 3a), we measured the traveltime t between the upper ultrasonic transducer and the lower one by the transmission method at first. The round-trip time t_1 between the upper probe and upper interface (upper buffer/sample) and t_2 between the lower probe and lower interface (lower buffer/sample) was measured by the reflection. Using the corresponding phases to determine traveltime, the phase velocity

Table 1. Whole rock analysis and chemical compositions of minerals in the amphibolite.

Oxides	Amphibolite	Amphibole (8)		Biotite (5)		Plagioclase (5)	
	XRF	EMP	SD	EMP	SD	EMP	SD
SiO ₂	47.75	47.59	2.58	41.60	0.25	58.61	1.28
TiO ₂	1.00	0.95	0.54	1.35	0.02	0.01	0.02
Al ₂ O ₃	15.78	8.21	3.39	15.55	0.06	25.41	0.46
FeO*	9.78	12.70	1.75	15.28	0.22	0.41	0.58
MnO	0.20	0.24	0.08	0.34	0.03	0.06	0.09
MgO	7.65	12.25	1.64	14.99	0.29	0.02	0.02
CaO	11.25	12.16	0.79	0.04	0.00	6.68	0.72
Na ₂ O	2.48	1.33	0.60	0.12	0.04	8.92	0.56
K ₂ O	1.09	0.60	0.29	5.88	0.11	0.18	0.04
P ₂ O ₅	0.26	–	–	–	–	–	–
LOI	2.00	–	–	–	–	–	–
Total	99.24	96.08	1.32	95.19	0.20	100.30	0.31

Mineralogical composition:

58.4 per cent amphibole + 9.2 per cent biotite + 32.3 per cent plagioclase + epidote + magnetite + sphene + apatite (<1 per cent), by point counting analysis (1500 points).

Amphibole 60.8 wt. per cent + biotite 7.7 wt. per cent + plagioclase 31.5 wt. per cent, by mass balance calculation (Fisher 1993).

Density: 2.876 g cm⁻³. Porosity: <1.0 per cent.

Note: XRF, X-ray fluorescence analysis; EMP, electron microprobe analysis; SD, standard of deviation; LOI, loss on ignition; –, no detection. All the values are in wt. per cent. The number in the parentheses behind the mineral is points analysed.

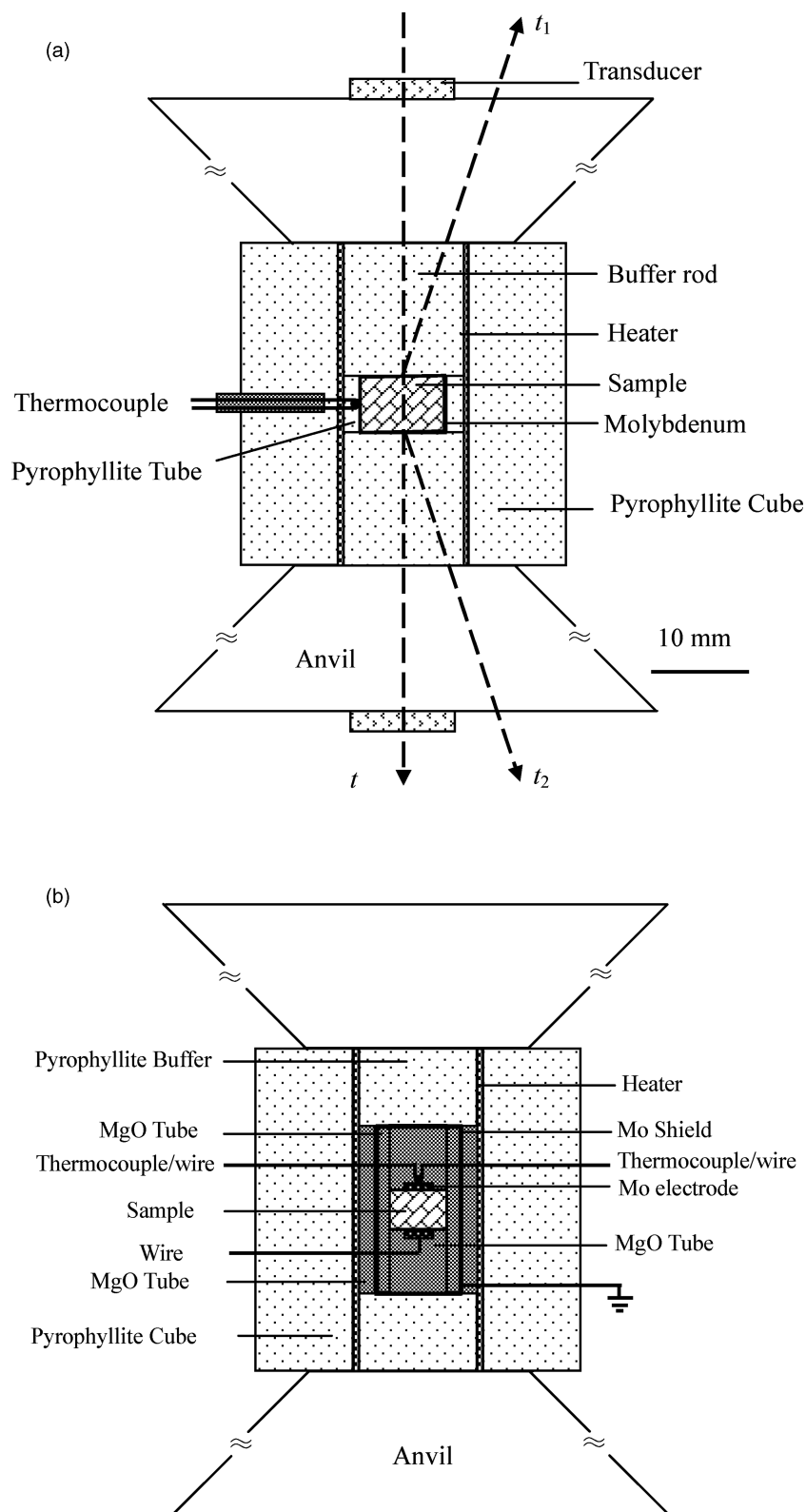


Figure 3. Schematic cross-sections of the sample assembly for elastic wave velocity (a) and electrical conductivity measurements (b). The dash lines indicate the traveltime t between the upper ultrasonic transducer and the lower one, the round-trip time t_1 between the upper probe and upper interface (upper buffer/sample) and t_2 between the lower probe and lower interface.

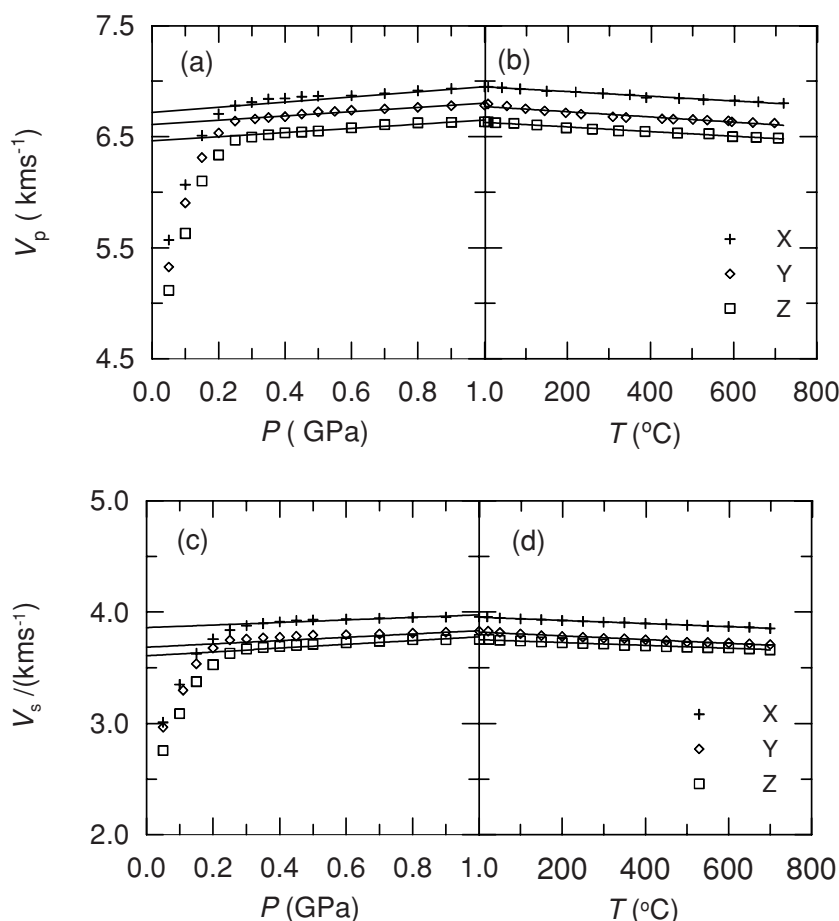


Figure 4 Wave velocities in the amphibolite. As a function of (a, c) pressure at room temperature and (b, d) temperature at 1.0 GPa. The lines represent linear fits to V_p and V_s versus P data in the range of 0.25–1.0 GPa and extrapolations to zero pressure in a and c, and versus T data in b and d. X is the sample parallel to lineation, Y is the perpendicular to lineation in foliation and Z is the normal to foliation.

was obtained. The precision of timing measurement is ± 2 ns. The traveltime of the sample (t_s) was calculated from the formula $t_s = t - t_1/2 - t_2/2 - t_c$, in which t_c is the correction time for two 0.1 mm molybdenum foils. The correction time was calculated after the thermoelastic equation of state of molybdenum at atmosphere (Zhao *et al.* 2000).

The length correction of the sample at pressure was based on the method of Cook (1957) by using the formula $L/L_0 = 1 - (p/(3K_0))$, in which L is the length of the sample at pressure, L_0 is the length at atmosphere, p is the pressure and K_0 is the bulk modulus (51.0 GPa). Finally, the V_p and V_s was calculated by the formula $V_p(V_s) = L/t_s$. The maximum error of this method is less than 1.2 per cent (Liu *et al.* 2002).

We determined the electrical conductivities (σ) in the amphibolite with the impedance spectroscopy. For impedance spectroscopy, we used a Solartron 1260 impedance/gain phase analyser with 1 V applied voltage over the frequency range 1.0 MHz to 0.05 Hz. The sample assemblage for electrical conductivity measurements is shown in Fig. 3(b). Mo electrodes and an Mo shield connected to ground were used for keeping the oxygen fugacity closed to the Mo–MoO₂ buffer and reducing the leakage currents. Detailed descriptions of the conductivity measurement have been given by Zhu *et al.* (2001), Wang *et al.* (2008) and Dai *et al.* (2008). The method used here is also similar with the method of Xu *et al.* (1998).

In all experiments, the pressure was raised at a rate of 4×10^5 Pa s^{-1} . For elastic wave velocity, measurements were taken at room

temperature for high pressure at 0.05–0.10 GPa steps firstly. After these measurements were finished, the pressure was kept at 1.0 GPa for 20 min and then the temperature was increased at a rate of 0.6 $^{\circ}\text{C s}^{-1}$ to the desired temperature. The elastic wave velocities were taken at 50 $^{\circ}\text{C}$ step from 50 to 700 $^{\circ}\text{C}$. At each temperature, the annealing time was 30 min. For electrical conductivity, the measurements were performed at 1.0 GPa. The sample assembly was kept at 1.0 GPa and 700 $^{\circ}\text{C}$ for more than 10 h to obtain the stabilized resistance before the impedance spectroscopy were taken at 50 $^{\circ}\text{C}$ step from 700 to 250 $^{\circ}\text{C}$. At each temperature, the annealing time was 1 h. The oxygen fugacity during the experiments is believed to close to the Mo–MoO₂ buffer (Xu *et al.* 1998). We checked the recovered samples (Fig. 2b) and no mineral reactions were found.

3 RESULTS AND DISCUSSION

3.1 Elastic wave velocity

In Fig. 4(a) and (c), the V_p and V_s in the three directions of amphibolite are shown as a function of pressures in the range of 0.05–1.0 GPa at room temperature, respectively. In Fig. 4(b) and (d), both the V_p and V_s are shown as a function of temperatures from room temperature to 700 $^{\circ}\text{C}$ at 1.0 GPa, respectively. As showing in Fig. 4, elastic wave velocities increase in the structural directions Z , Y , X . At room temperature, elastic wave velocities increase rapidly with

Table 2. Elastic wave velocities (V_{p0} and V_{s0}) and bulk and shear modulus of the crack-free amphibolite at zero pressure, and the pressure and temperature derivatives of elastic wave velocities.

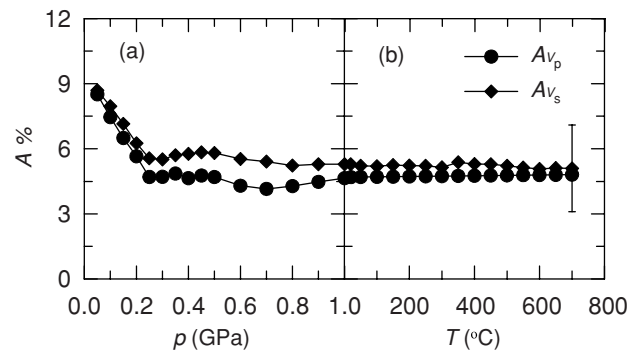
Direction	V_0 (km s ⁻¹)	$(\partial V/\partial p)_T$ (km s ⁻¹ GPa ⁻¹)	P (GPa)	$(\partial V/\partial T)_p$ (km s ⁻¹ °C ⁻¹)	T (°C)
V_p					
X	6.719	0.2308	0.25–1.00	–0.000211	20–700
Y	6.610	0.1915	0.25–1.00	–0.000235	20–700
Z	6.462	0.1883	0.25–1.00	–0.000209	20–700
Average	6.599	0.1975	0.25–1.00	–0.000218	20–700
V_s					
X	3.859	0.1149	0.25–1.00	–0.000143	20–700
Y	3.682	0.1488	0.25–1.00	–0.000168	20–700
Z	3.608	0.1678	0.25–1.00	–0.000128	20–700
Average	3.716	0.1438	0.25–1.00	–0.000147	20–700
Bulk modulus (K , GPa)	72.3	Shear modulus (μ , GPa)		39.7	

increasing pressure at pressures lower than 0.25 GPa (Fig. 4a and c). At pressures range from 0.25 to 1.0 GPa, elastic wave velocities increase linearly with pressure, which is thought to reflect the intrinsic pressure sensitivity of the crack-free material (Kern *et al.* 1999; Zhao *et al.* 2001). The velocities at 1.0 GPa in the three structural directions of the amphibolite are 6.63 km s⁻¹ (Z), 6.78 km s⁻¹ (Y) and 6.95 km s⁻¹ (X) for V_p , and 3.75 km s⁻¹ (Z), 3.82 km s⁻¹ (Y) and 3.96 km s⁻¹ (X) for V_s . The pressure coefficients of the sample, obtained by the linear regression based on the data of 0.25–1.0 GPa, are in the range of 0.1883–0.2308 km s⁻¹ GPa⁻¹ for V_p and 0.1149–0.1678 km s⁻¹ GPa⁻¹ for V_s (Table 2). The pressure coefficients of V_s are consistent with the results of Kern *et al.* (1993, 1996, 1999), who got the pressure coefficients of V_s in the range of 0.0721–0.1990 km s⁻¹ GPa⁻¹ at room temperature and pressures up to 0.7 GPa. However, the pressure coefficients of V_p are lower than the results of Kern *et al.* (0.282–0.659 km s⁻¹ GPa⁻¹) (Kern *et al.* 1993, 1996, 1999). Perhaps, the difference in experimental pressure range is responsible for such an inconsistency. Elastic wave velocities (V_{p0} and V_{s0}) of the crack-free amphibolite at zero pressure were calculated according to the linear regression formula (Table 2).

Elastic wave velocities in the amphibolite decrease linearly with increasing temperature at 1.0 GPa (Fig. 4b and d). The temperature coefficients obtained by the linear regression are in the range of $2.09\text{--}2.35 \times 10^{-4}$ km s⁻¹ GPa⁻¹ for V_p and $1.28\text{--}1.68 \times 10^{-4}$ km s⁻¹ GPa⁻¹ for V_s (Table 2). The results are consistent with those of previous studies (Kern *et al.* 1993, 1996, 1999).

The amphibolite exhibits pronounced velocity anisotropy. The velocity anisotropy can be calculated with velocities in the three structural directions (X , Y , Z). The coefficient of anisotropy (A_v) is calculated with the formula of $A_v = (V_{\max} - V_{\min})/V_{\text{mean}}$ (Birch 1961). Fig. 5 presents velocity anisotropies (A_{V_p} and A_{V_s}) for the amphibolite as functions of pressure and temperature for V_p and V_s . It is widely accepted that the seismic anisotropy of rock is controlled by (1) the lattice preferred orientation (LPO), (2) the shape preferred orientation (SPO), (3) the preferred orientation of microcracks and (4) the thin mineral layers of different properties (Kern *et al.* 2001). Anisotropy is higher at pressures lower than 0.25 GPa. The pressure-dependent rapid increase of anisotropy results from the progressive close of oriented microcracks in this pressure range. Increasing pressure reduces the effect of oriented microcracks (Fig. 5a). At pressure higher than 0.25 GPa, the effect of oriented microcracks is almost eliminated and the residual (intrinsic) anisotropy may be mainly due to the LPO, SPO and thin mineral layers (Siegesmund *et al.* 1989; Kern & Wenk 1990; Ji & Salisbury 1993; Barruol & Kern 1996). In our amphibolite, the aspect ratios of amphibole, plagioclase and biotite are about 1.6:1.3:1.0, 1.3:1.1:1.0 and 1.9:1.2:1.0 in the three structural directions. The aspect ratios of amphibole and plagioclase are relatively small. Although biotite grains have the relatively large aspect ratios, the modal composition of biotite is only about 7.7–9.2 per cent. Therefore, we believed that the SPO may not be an important reason for the seismic anisotropy of the amphibolite at pressure of 0.25–1.0 GPa. The amphibolite also exhibits pronounced banding defined by plagioclase– and amphibole + biotite layers. The results of Siegesmund *et al.* (1989) and Ji *et al.* (1993) indicated that the mineral banding may have little effect on the anisotropy. Almost all previous studies showed that the measured P -wave anisotropy of the amphibolite is roughly comparable to that calculated data, based on the LPO and the single crystal velocities of the mineral constituents in the amphibolite. Kern *et al.* (2001), for example, observed similar velocity–pressure relations on the biotite-hornblende gneiss sampled in the Kola superdeep borehole. They showed that experimentally determined intrinsic velocities observed in the three structural directions X , Y , Z , and resulting anisotropies (22.5 per cent) compare fairly well with corresponding calculated data (25.6%). Therefore, we believed that the LPO of the mineral constituents in the amphibolite is a major contribution to the intrinsic seismic anisotropy. The residual anisotropy at room temperature in the pressure range of 0.25–1.0 GPa is 4.15–4.86% for V_p and 5.29–5.84% for V_s . At 1.0 GPa, A_{V_s} showed a slight decrease (from 5.29 to 5.10 per cent) and A_{V_p} showed a slight increase (from 4.69 to 4.81 per cent) with temperature (Fig. 7b) because the confining pressure of 1.0 GPa is high enough to prevent thermal cracking (Kern & Richter 1981).

class and biotite are about 1.6:1.3:1.0, 1.3:1.1:1.0 and 1.9:1.2:1.0 in the three structural directions. The aspect ratios of amphibole and plagioclase are relatively small. Although biotite grains have the relatively large aspect ratios, the modal composition of biotite is only about 7.7–9.2 per cent. Therefore, we believed that the SPO may not be an important reason for the seismic anisotropy of the amphibolite at pressure of 0.25–1.0 GPa. The amphibolite also exhibits pronounced banding defined by plagioclase– and amphibole + biotite layers. The results of Siegesmund *et al.* (1989) and Ji *et al.* (1993) indicated that the mineral banding may have little effect on the anisotropy. Almost all previous studies showed that the measured P -wave anisotropy of the amphibolite is roughly comparable to that calculated data, based on the LPO and the single crystal velocities of the mineral constituents in the amphibolite. Kern *et al.* (2001), for example, observed similar velocity–pressure relations on the biotite-hornblende gneiss sampled in the Kola superdeep borehole. They showed that experimentally determined intrinsic velocities observed in the three structural directions X , Y , Z , and resulting anisotropies (22.5 per cent) compare fairly well with corresponding calculated data (25.6%). Therefore, we believed that the LPO of the mineral constituents in the amphibolite is a major contribution to the intrinsic seismic anisotropy. The residual anisotropy at room temperature in the pressure range of 0.25–1.0 GPa is 4.15–4.86% for V_p and 5.29–5.84% for V_s . At 1.0 GPa, A_{V_s} showed a slight decrease (from 5.29 to 5.10 per cent) and A_{V_p} showed a slight increase (from 4.69 to 4.81 per cent) with temperature (Fig. 7b) because the confining pressure of 1.0 GPa is high enough to prevent thermal cracking (Kern & Richter 1981).

**Figure 5.** Anisotropy of elastic wave velocity in the amphibolite. As a function of (a) pressure at room temperature and (b) temperature at 1.0 GPa. A_{V_p} , anisotropy of compressional wave velocity; A_{V_s} , anisotropy of shear wave velocity. Error bar corresponds to the maximum error.

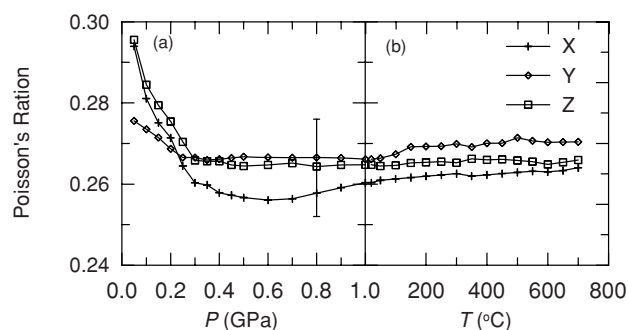


Figure 6. Poisson's ratio in the amphibolite. As a function of (a) pressure at room temperature and (b) temperature at 1.0 GPa. Error bar corresponds to the maximum error. X is the sample parallel to lineation, Y is the perpendicular to lineation in foliation and Z is the normal to foliation.

In Fig. 6, we plotted the Poisson ratio against pressure at room temperature and temperature at 1.0 GPa. At pressures lower than 0.25 GPa, the Poisson ratio decreases markedly with increasing pressure. In the pressure range of 0.25–1.0 GPa, the Poisson ratio

shows a small variation. At pressure of 1.0 GPa, the Poisson ratio increases slowly with increasing temperature. The Poisson ratio for the amphibolite is consistent with the results of previous studies (0.262–0.316, Kern *et al.* 1993, 1996, 1999; $(0.260\text{--}0.265) \pm 0.017$, Christensen 1996).

3.2 Electrical conductivity

Fig. 7 shows the complex impedance curves for the structural direction X in the amphibolite at 1.0 GPa and 250–700 °C, together with the equivalent circuit in the inset of Fig. 7(a). The complex impedance curve shows a semicircular arc and a small tail in our experimental temperature and frequency ranges. The complex impedance curves for the structural directions Y and Z are similar. It is observed that the intercept of these semicircles on real axis shifts towards origin at higher temperatures. Also the centre of these semicircles is depressed below the real axis. According to Roberts & Tyburczy (1994) and Huebner & Dillenaug (1995), the semicircular arc in Fig. 7 is due to grain interior processes and can characterize the intrinsic conduction mechanism of the sample

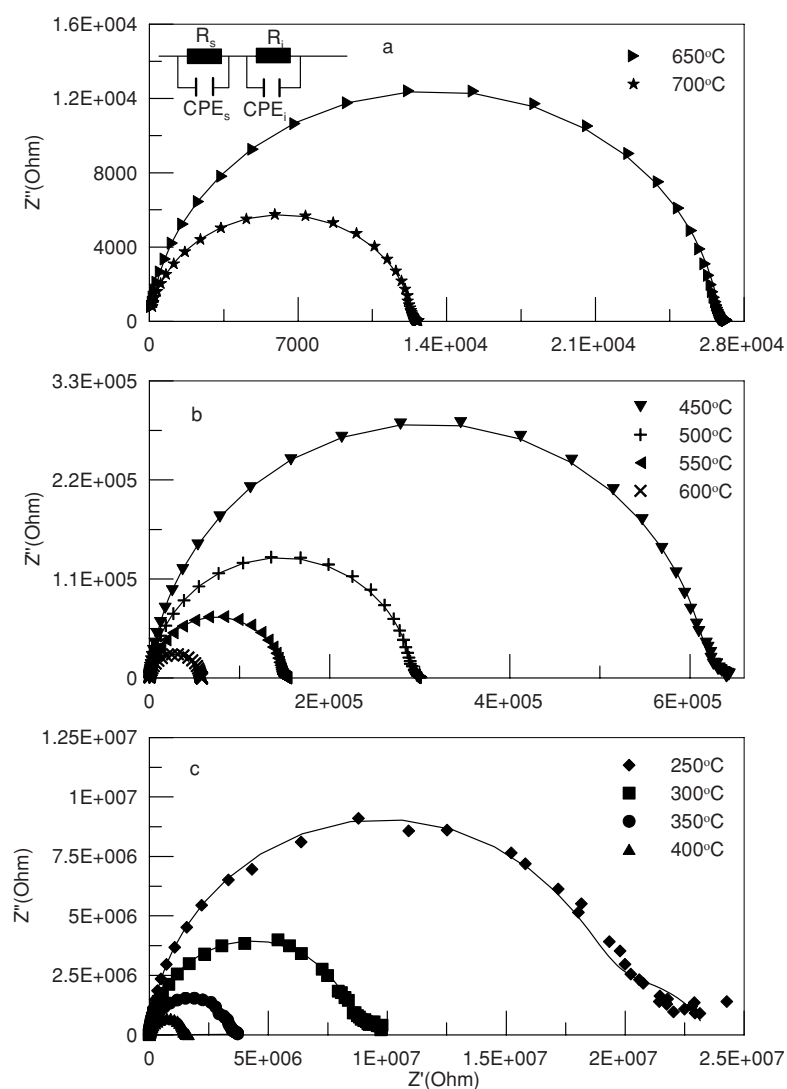


Figure 7. Impedance spectroscopy for the sample of the structural direction X in the amphibolite at 1.0 GPa and 250–700 °C. The equivalent circuit with parameters of sample resistance (R_s), sample constant phase element (CPE_s), interaction resistance between the sample and the electrode (R_i), and interaction constant phase element between the sample and the electrode (CPE_i) is shown in the inset of a.

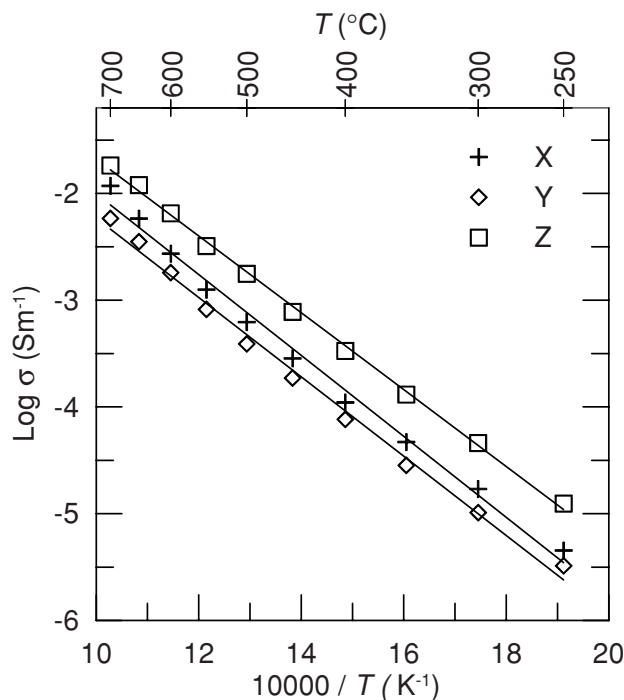


Figure 8. Electrical conductivity versus $1/T$ at 1.0 GPa in the amphibolite. The lines are the Arrhenius plots. X is the sample parallel to lineation, Y is the perpendicular to lineation in foliation and Z is the normal to foliation.

and the diameter of the semicircular arc stands for the DC intrinsic resistance of the sample. The tail is interpreted as the interaction between the sample and the electrode. Therefore, in present experiments, grain interior mechanism is dominant in the electrical conductivity. Fitting the impedance spectroscopy in Fig. 7 with the equivalent circuits with parameters of sample resistance (R_s), sample constant phase element (CPE_s), interaction resistance between the sample and the electrode (R_i) and interaction constant phase element between the sample and the electrode (CPE_i) (inset in Fig. 7a) by using Z-view program software, we worked out the R_s . The conductivity was then calculated using the sample dimensions. Fitting errors are less than 1 per cent for each resistance at a given temperature. The dimensional change of the sample and electrode is negligible in our experimental pressure and temperature range. Estimated maximum error for electrical conductivity is less than 2 per cent.

The logarithm of electrical conductivity in the amphibolite at 1.0 GPa is displayed as a function of reciprocal temperature in Fig. 8. The three samples show similar conductivity behaviour and the conductivity increases in the structural directions Y , X and Z . The electrical conductivity increases with increasing temperature, which is consistent with the Arrhenius relationship. The Arrhenius relationship is in the form of $\sigma = \sigma_0 \exp(-\Delta E/(kT))$, where σ is the electrical conductivity ($S m^{-1}$), σ_0 is the pre-exponential factor approximately independent of temperature ($S m^{-1}$), ΔE is the activation energy (eV), k is the Boltzmann constant ($eV K^{-1}$) and T is the absolute temperature (K). We acquired parameters for the electrical conductivity of the amphibolite by fitting the conductivity data to Arrhenius relationship formula (Table 3).

Activation energies for the three structural directions of the amphibolite are similar and in the range of 0.71–0.75 eV, which is closed to the activation energy of gabbro (0.67 eV, Wang *et al.* 2002). However, the activation energy is higher than that of gneiss

Table 3 Parameters of the Arrhenius formula.

Direction	p (GPa)	T (K)	σ_0 ($S m^{-1}$)	ΔE (eV)
X	1.0	523–973	61.67 ± 0.40	0.75 ± 0.03
Y	1.0	523–973	30.59 ± 0.33	0.74 ± 0.02
Z	1.0	523–973	83.06 ± 0.17	0.71 ± 0.01
Average	1.0	523–973	53.91 ± 0.29	0.73 ± 0.02

(0.24–0.27 eV, Fuji-ta *et al.* 2007) and is lower than that of granulite (1.40 eV, Partzsch *et al.* 2000) and lherzolite (1.46 eV, Duba *et al.* 1993).

The amphibolite shows electrical conductivity anisotropy. The electrical conductivities for the three structural directions show a maximum difference of about 0.6 log units. The electrical conductivity anisotropy was calculated after the method used in the calculation of velocity anisotropy. The formula for calculating the coefficient of anisotropy (A_σ) is $A_\sigma = (\log \sigma_{\max} - \log \sigma_{\min}) / \log \sigma_{\text{mean}}$. Fig. 9 presents electrical conductivity anisotropies for the amphibolite as a function of temperature at 1.0 GPa. Electrical conductivity anisotropy increases with increasing temperature, which is 11.1 per cent at 250 °C and 25.2 per cent at 700 °C. Why the data point at 500 °C is out of the error range is not clear. There is not a firm conclusion for the electrical conductivity anisotropy. Siegesmund *et al.* (1991) inferred that the anisotropy of electrical conductivity in the mylonitic clinopyroxene amphibolite and epidote–muscovite–quartz ultramylonite can be explained by the geometry of crack system, rock fabric and interaction between the fluid pore electrolyte and the solid mineral phase. The results of Glove & Vine (1992) indicated that the anisotropy of electrical conductivity in the carbon-bearing granulite depends on the orientation of the carbon-bearing foliation. Fuji-ta *et al.* (2007) believed that in neither pore fluid nor saturated saline water rock, the electrical conductivity anisotropy was due to the alignment of the relatively conductive minerals in certain orientations. In the case of our experiments, we used dried samples and did not find any graphite among mineral grains, so the electrical conductivity anisotropy was not due to the orientation of fluid and graphite. The alignment of the amphibole and biotite may

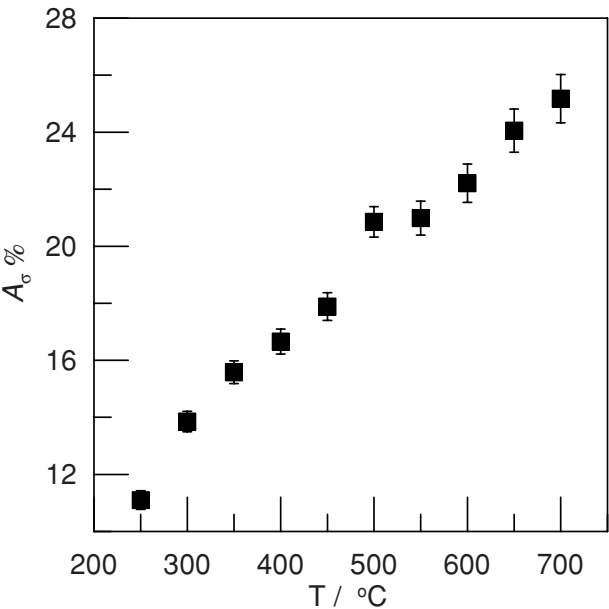


Figure 9. Anisotropy of electrical conductivity in the amphibolite (A_σ) as a function of temperature at 1.0 GPa.

Table 4. Thermal parameters, layer thickness and boundary conditions of the four-layer crust model for the Tarim Basin.

No.	Layer	Thickness (z , km)	Heat production rate (A , $\mu\text{W m}^{-3}$)	Thermal conductivity (κ , $\text{W m}^{-1}\text{K}^{-1}$)	Density (ρ , g cm^{-3})
1	Sediment	10 ^a	1.30 ^b	2.32 ^b	2.30 ^c
2	Upper crust	15 ^a	1.17 ^c	2.80 ^d	2.81 ^e
3	Middle crust	10 ^a	0.48 ^c	2.6 ^d	2.86 ^e
4	Lower crust	10 ^a	0.22 ^c	2.0 ^d	3.05 ^e

^a Shao & Zhang (1994), Shao *et al.* (1997), Zhang *et al.* (1998), Lu *et al.* (2000), Li *et al.* (2001), Gao *et al.* (2000), 2001.

^b Qiu (2002).

^c Wang *et al.* (1996).

^d Seipold (1992).

^e He *et al.* (2001).

be prominent in the electrical conductivity anisotropy. Whether it is true needs further investigation.

3.3 Calculation of velocity–depth profiles

The experimentally derived pressure and temperature derivatives, along with the zero-pressure velocities V_{p0} and V_{s0} (Table 2), were used to calculate velocities at various depths according to (Kern *et al.* 1999):

$$V(z) = V_0 + (\partial V / \partial p)_{T,p} + (\partial V / \partial T)_{p,T},$$

where $p = \rho g z$, p is pressure (GPa), ρ is density of rock (10^3 kg m^{-3}), g is gravitational acceleration (ms^{-2}), z is depth (m); $T = T_0 + z/\kappa \times (q_0 - A \times z/2)$, T is temperature ($^{\circ}\text{C}$), T_0 is the temperature of the regional surface ($^{\circ}\text{C}$), κ is specific thermal conductivity of rock ($\text{W m}^{-1} \text{K}^{-1}$), q_0 is regional surface heat flow (mW m^{-2}) and A is radiogenic heat production rate of rock ($\mu\text{W m}^{-3}$).

Several (wide-angle) reflection/refraction profiles pass through the western, middle and eastern Tarim Basin (Fig. 1). From west to east, they are Taxkorgan-Akqi profile (AA' in Fig. 1, Zhang *et al.* 2002), Aksu-Yecheng profile (BB' in Fig. 1, Shao *et al.* 1997), Aral-Quanshuigou profile (CC' in Fig. 1, Li *et al.* 2001; Gao *et al.* 2001) and Kuqu-Tanan profile (DD' in Fig. 1, Shao *et al.* 1997). These profiles revealed a similar crustal structure model for the Tarim Basin (Shao *et al.* 1997; Li *et al.* 2001; Gao *et al.* 2001; Zhang *et al.* 2002), which is composed of four layers: a sediment layer with thickness of 3–15 km, an upper crust layer with thickness of 5–18

km, V_p of 5.90–6.20 km s^{-1} and V_s of 2.8–3.30 km s^{-1} , a middle crust layer with thickness of about 10 km, V_p of 6.20–6.70 km s^{-1} and V_s of 3.40–3.80 km s^{-1} , and a lower crust layer with thickness of about 10 km, V_p of 6.70–7.30 km s^{-1} and V_s of 3.60–4.00 km s^{-1} . The lateral variations of the thickness are very large for the sediment and the upper crust layers but small for the middle and lower crust layers.

The four layers crust model for the Tarim Basin was accepted in this calculation (Shao & Zhang 1994; Shao *et al.* 1997; Zhang *et al.* 1998), in which the crust is composed of a sediment layer (10 km), an upper crust layer (15 km), a middle crust layer (10 km) and a lower crust layer (10 km). The regional surface temperature is set to 15 $^{\circ}\text{C}$. The regional surface heat flow is 45 mW m^{-2} (Wang *et al.* 1995; Liu *et al.* 2004; Wang *et al.* 2001). The other parameters applied in the model are given in Table 4.

We calculated the average elastic wave velocities versus depth profiles of the amphibolite. Fig. 10 shows the experimentally derived velocity–depth profiles, along with the velocity–depth profile for the crust, obtained by the seismic survey (Shao & Zhang 1994; Shao *et al.* 1997). The V_p of the amphibolite passes through the lower boundary of middle crust velocity range and the upper boundary of lower crust velocity range. The V_s of the amphibolite also passes through the lower boundary of middle crust velocity range. However, it traverses the middle of lower crust velocity range. Based on the comparison, it is reasonable to speculate that the amphibolite is probably one of the constituents in middle or lower crust of the Tarim Basin.

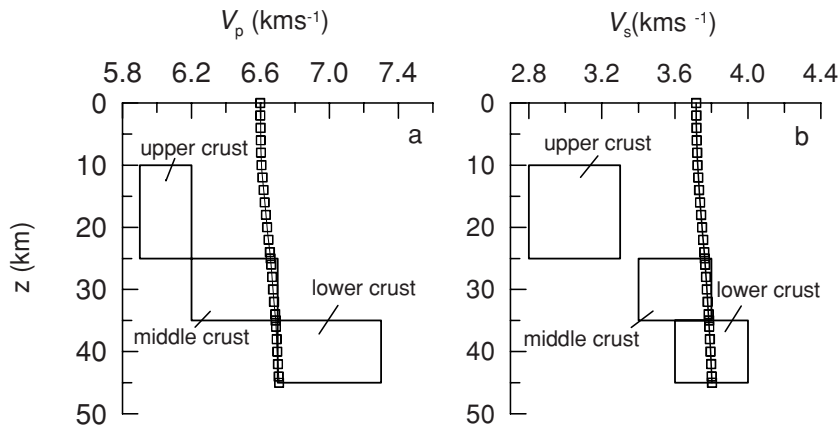


Figure 10. Elastic wave velocity versus depth profiles for the amphibolite based on the experimental data, along with the velocity profiles obtained by seismic survey (Shao & Zhang 1994; Shao *et al.* 1997). (a) P -wave velocity versus depth profiles and (b) S -wave velocity versus depth profiles.

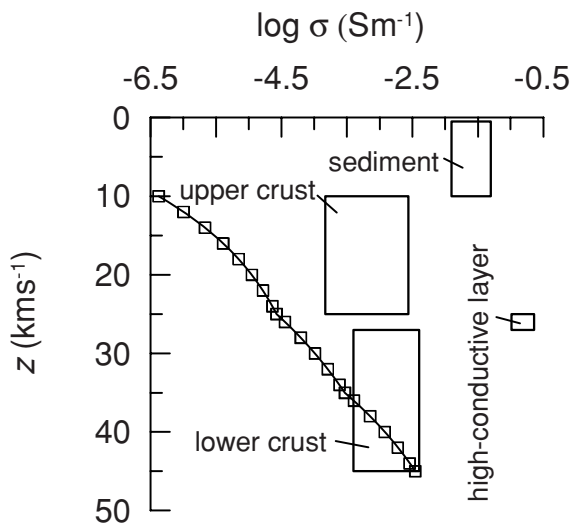


Figure 11. Electrical conductivity versus depth profiles for the amphibolite based on the experimental data, along with the electrical conductivity profiles obtained by magnetotelluric survey (Qin *et al.* 1994; Lu *et al.* 1997).

3.4 Calculation of electrical conductivity–depth profile

We calculated the average electrical conductivity–depth profile of the amphibolite by using the Arrhenius relationship formula, the temperature–depth relationship described earlier.

Two magnetotelluric sounding profiles, the Aksu-Yecheng (BB' in Fig. 1) and the Aral-Quanshuigou (CC' in Fig. 1), pass through the Tarim Basin (Qin *et al.* 1994; Lu *et al.* 1997). The thin sheet modelling method has been used to construct a 2-D model. A three layers crust model was revealed by magnetotelluric sounding profiles for the Tarim Basin: a sediment layer with thickness of 3–12 km and $\log \sigma = -1.3$ to -1.9 S m $^{-1}$, an upper crust layer with thickness of 6–22 km and $\log \sigma = -2.56$ to -3.83 S m $^{-1}$ and a lower crust layer with thickness of 15–25 km and $\log \sigma = -2.40$ to -3.40 S m $^{-1}$. Between the upper crust layer and the lower crust layer, there is a high-conductive layer with thickness of 2 km and $\log \sigma = -0.64$ to -0.99 S m $^{-1}$. The sediment and upper crust layers of the Tarim Basin derived from the magnetotelluric sounding data is roughly consistent with that with seismic data. However, the middle crust and lower crust layers obtained from seismic data cannot be resolved with the magnetotelluric sounding data.

Compared with the crust model of the Tarim Basin revealed by magnetotelluric sounding profiles (Qin *et al.* 1994; Lu *et al.* 1997), the three layers crust model used in this calculation did not take the high-conductive layer into account. The three layers crust model is composed of a sediment layer (10 km), an upper crust layer (15 km) and a lower crust layer (20 km). Thermal parameters and densities of the sediment and upper crust layers are the same as used in the velocity–depth calculation. The heat production rate, thermal conductivity and density of the lower crust are $0.35 \mu\text{W m}^{-3}$, $2.3 \text{ W m}^{-1} \text{ K}^{-1}$, and 2.96 g cm^{-3} , respectively. We ignored the effect of pressure on the electrical conductivity during the calculation, because the pressure has little effect on the electrical conductivity at pressures lower than 1.0 GPa (Nover 2004). Fig. 11 shows the experimentally derived electrical conductivity–depth profile, along with the electrical conductivity–depth profile for the crust obtained by the magnetotelluric survey (Qin *et al.* 1994; Lu *et al.* 1997). The electrical conductivity of the sample increases with increasing depth. At the depth of 10 km corresponding to the top of upper crust in the three layers crust model, the electrical conductivity of

the sample is -6.3 log units. At the depth of 45 km, the bottom of lower crust, the electrical conductivities of the sample is -2.4 log units. As showing in Fig. 11, the electrical conductivity is in the electrical conductivity range of the lower crust, which may indicate that the amphibolite is probably one of the constituents of the lower crust. Because the lower crust of the three layers crust model is roughly equivalent to the middle and lower crust layers of the four layers crust model used in the velocity–depth calculation, the conclusion is consistent with the deduction derived from the comparison of experimental velocity with the seismic survey.

4 CONCLUSION

We have measured the elastic wave velocities and electrical conductivities in three structural directions (normal to foliation Z , perpendicular to lineation in foliation Y and parallel to lineation X) of an amphibolite exposed in the southwestern margin of the Tarim Basin, northwest China, as a function of pressure and temperature. Both of the experimental elastic wave velocities and electrical conductivities are compared with the field geophysical investigation. We obtained the compressional (V_p) and shear wave velocities (V_s), velocity anisotropy (A_v), electrical conductivity (σ) and electrical anisotropy (A_σ) of the amphibolite at pressures to 1.0 GPa and temperatures to 700 °C. The velocities at 1.0 GPa in the three structural directions of the amphibolite are 6.63 km s^{-1} (Z), 6.78 km s^{-1} (Y), and 6.95 km s^{-1} (X) for V_p , and 3.75 km s^{-1} (Z), 3.82 km s^{-1} (Y), and 3.96 km s^{-1} (X) for V_s , respectively. Velocity anisotropy is pronounced in the amphibolite. The anisotropy mainly due to the LPO at room temperature and 1.0 GPa is 4.15 per cent for V_p and 5.29 per cent for V_s . The electrical conductivity increases in the structural directions Y , X and Z , and varies by about 0.6 log units at the experimental temperature range. Electrical conductivity anisotropies (A_σ) are in the range of 11.1–25.2 per cent. Based on the comparison of the experimental results with those of field geophysical investigations, it is evident that the V_p , V_s and σ of the sample is consistent with those of the middle or lower crust (or the lower crust of the crust model obtained by the magnetotelluric survey). A possible interpretation is that the amphibolite is one of the constituents of the middle crust or lower crust of the Tarim Basin.

ACKNOWLEDGMENTS

The manuscript was substantially improved by Hartmut Kern and four anonymous reviewers. This work is supported by the National Natural Science Foundation of China (Grant No. 40873052), the 'Western Light' Project and Youth innovative foundation of the Chinese Academy of Sciences and the Knowledge Innovation Project of the Chinese Academy of Science (Grant No. KJCX2-SW-N20).

REFERENCES

- Aizawa, Y., Ito, K. & Tatsumi, Y., 2002. Compressional wave velocity of granite and amphibolite up to melting temperatures at 1 GPa, *Tectonophysics*, **361**, 255–261.
- Barrool, G. & Kern, H., 1996. Seismic anisotropy and shear-wave splitting in lower-crustal and upper-mantle rocks from the Ivrea zone-experimental and calculated data. *Phys. Earth planet. Inter.*, **95**, 175–194.
- Behn, M.D. & Kelemen, P.B., 2003. Relationship between seismic P-wave velocity and the composition of anhydrous igneous and meta-igneous rocks, *Geochim. Geophys. Geosyst.*, **4**, doi:10.1029/2002GC000393.
- Birch, F., 1960. The velocity of compressional waves in rocks to 10 kilobar: Part 1, *J. geophys. Res.*, **65**, 1083–1102.

- Birch, F., 1961. The velocity of compressional waves in rocks to 10 kilobar: Part 2, *J. geophys. Res.*, **66**, 2199–2224.
- Burke, M.M. & Fountain, D.M., 1990. Seismic properties of rocks from an exposure of extended continental crust—new laboratory measurements from the Ivrea zone, *Tectonophysics*, **182**, 119–146.
- Christensen, N.I., 1965. Compressional wave velocities in metamorphic rocks at pressures to 10 kilobars, *J. geophys. Res.*, **70**, 6147–6164.
- Christensen, N.I., 1966. Shear-wave velocities in metamorphic rocks at pressures to 10 kbar, *J. geophys. Res.*, **71**, 3549–3556.
- Christenson, N.I. & Fountain, D.M., 1975. Constitution of the lower continental crust based on experimental studies of seismic velocity in granulite, *Geol. Soc. Am. Bull.*, **86**, 227–236.
- Christensen, N.I., 1996. Poisson's ratio and crustal seismology, *J. geophys. Res.*, **101**, 3139–3156.
- Christensen, N.I. & Mooney, N.D., 1995. Seismic velocity structure and composition of the continental crust: a global view, *J. geophys. Res.*, **100**, 9761–9788.
- Chroston, P.N. & Evans, C.J., 1983. Seismic velocities of granulites from the Seiland petrographic province, Norway: implications for Scandinavian lower continental crustal, *J. Geophys.*, **52**, 14–21.
- Cook, R.K., 1957. Variation of elastic constants and static strains with hydrostatic pressure: a method for calculation from ultrasonic measurements, *J. acoust. Soc. Am.*, **29**, 445–449.
- Dai, L., Li, H., Hu, H. & Shan, S., 2008. Experimental study of grain boundary electrical conductivities of dry synthetic peridotite under high-temperature, high-pressure, and different oxygen fugacity conditions, *J. geophys. Res.*, **113**, B12211, doi:10.1029/2008JB005820.
- Ding, D.G., Wang, D.X., Liu, W.X. & Sun, S.Q., 1996. *The West Kunlun Orogen and Basins* (in Chinese), Geological Publishing House, Beijing.
- Duba, A., 1993. The electrical conductivity of lherzolite, *J. geophys. Res.*, **98**, 11 885–11 899.
- Fisher, G.W., 1993. An improved method of algebraic analysis of metamorphic mineral assemblages. *Am. Mineral.*, **78**, 1257–1261.
- Freund, F., 2003. On the electrical conductivity structure of the stable continental crust, *J. Geodyn.*, **35**, 353–388.
- Frost, B.R., Fyfe, W.S., Tazaki, K. & Chan, T., 1989. Grain-boundary graphite in rocks and implications for high electrical conductivity in the lower crust, *Nature*, **340**, 134–136.
- Fuji-ta, K., Katsura, T. & Tainosho, Y., 2004. Electrical conductivity measurement of granulite under mid- to lower crustal pressure-temperature conditions, *Geophys. J. Int.*, **157**, 79–86.
- Fuji-ta, K., Katsura, T., Matsuzaki, T., Ichiki, M. & Kobayashi, T., 2007. Electrical conductivity measurement of gneiss under mid- to lower crustal P–T conditions, *Tectonophysics*, **434**, 93–101.
- Gao, R., Huang, D., Lu, D., Qian, G., Li, Y., Kuang, C. & Li, Q., 2000. Deep seismic reflection profile across the juncture zone between the Tarim Basin and the West Kunlun Mountains, *Chinese Sci. Bull.*, **45**, 2281–2286.
- Gao, R., Xiao, X., Liu, X., Guan, Y., Li, Q., Lu, D. & Li, P., 2001. Detail lithospheric structure of the contact zone of West Kunlun and Tarim revealed by deep seismic reflection profile along the Xinjiang Geotransect, *Acta Geosci. Sin.*, **22**, 547–552 (in Chinese with English abstract).
- Gao, S., Zhang, B.R., Jin, Z.M., Kern, H., Luo, T.C. & Zhao, Z.D., 1998. How mafic is the lower continental crust? *Earth planet. Sci. Lett.*, **161**, 101–117.
- Glover, P.W. & Vine, F.J., 1992. Electrical conductivity of carbon-bearing granulite at raised temperatures and pressures, *Nature*, **360**, 723–726.
- He, R., Gao, R., Li, Q., Guan, Y. & Li, P., 2001. Corridor gravity fields and crustal density structures in Tianshan (Dushanzi)-West Kunlun (Quanshuigou) GGT, *Acta Geosci. Sin.*, **22**, 553–558 (in Chinese with English abstract).
- Huebner, S.J. & Dillenaug, G.D., 1995. Impedance spectra of dry silicate minerals and rock: qualitative interpretation of spectra, *Am. Miner.*, **80**, 46–64.
- Hyndman, R.D. & Klempner, S.L., 1989. Lower-crustal porosity from electrical measurements and inferences about composition from seismic velocities, *Geophys. Res. Lett.*, **16**, 255–258.
- Ito, K. & Tsurumi, Y., 1995. Measurement of elastic velocities in granulite and amphibolite having identical H₂O free bulk compositions up to 850°C at 1 GPa, *Earth planet. Sci. Lett.*, **133**, 255–264.
- Ji, S. & Salisbury, M., 1993. Shear-wave velocities, anisotropy and splitting in the high grade mylonites, *Tectonophysics*, **221**, 453–473.
- Ji, S., Salisbury, M.H. & Hammer, S., 1993. Petrofabric, P-wave anisotropy and seismic reflectivity of high-grade tectonites, *Tectonophysics*, **222**, 195–226.
- Kariya, K.A. & Shankland, T.J., 1983. Electrical conductivity of dry lower crust rocks. *Geophysics*, **48**, 52–61.
- Kern, H. & Richter, A., 1981. Temperature derivatives of compressional and shear wave velocities in crustal and mantle rocks at 6 kbar confining pressure, *J. Geophys.*, **49**, 47–56.
- Kern, H. & Schenk, V., 1988. A model of velocity structure beneath Calabria, southern Italy, based on laboratory data, *Earth planet. Sci. Lett.*, **87**, 325–337.
- Kern, H. & Wenk, H.R., 1990. Fabric-related velocity anisotropy and shear-wave splitting in rocks from the Santa Rosa mylonite zone, California, *J. geophys. Res.*, **95**, 11212–11223.
- Kern, H., Walther, Ch., Fluh, E.R. & Maoker, M., 1993. Seismic properties of rocks exposed in the POLAR profile region—constraints on the interpretation of the refraction data. *Precambrian Res.*, **47**, 205–221.
- Kern, H., Gao, S. & Liu, Q., 1996. Seismic properties and densities of middle and lower crustal rocks exposed along the North China Geoscience Transect, *Earth planet. Sci. Lett.*, **139**, 439–455.
- Kern, H., Gao, S., Jin, Z., Popp, T. & Jin, S., 1999. Petrophysical studies on rocks from the Dabie ultrahigh-pressure (UHP) metamorphic belt, Central China: implications for the composition and delamination of the lower crust, *Tectonophysics*, **301**, 191–215.
- Kern, H., Popp, T., Gorbatshev, F., Zharikov, A., Lobanov, K.V. & Smirnov, Yu.P., 2001. Pressure and temperature dependence of V_p and V_s in rocks from the superdeep well and from surface analogues at Kola and the nature of velocity anisotropy, *Tectonophysics*, **338**, 113–134.
- Kern, H., Mengel, K., Strauss, K.W., Ivankina, T.I., Nikitin, A.N. & Kukkonen, I.T., 2009. Elastic wave velocities, chemistry and model mineralogy of crustal rocks sampled by the Outokumpu scientific drill hole: evidence from lab measurements and modeling, *Phys. Earth planet. Inter.*, **175**, 151–166.
- Kitamura, K., Ishikawa, M. & Arima, M., 2003. Petrological model of the northern Izu-Bonin-Mariana arc crust: constraints from high-pressure measurements of elastic wave velocities of the Tanzawa plutonic rocks, central Japan, *Tectonophysics*, **371**, 213–221.
- Li, J. & Xiao, X., 1999. A brief commentary on several problems of the crustal structure and tectonic evolution of Xinjiang, *Scientia Geologica Sinica*, **34**, 405–419 (in Chinese with English abstract).
- Li, Q., Gao, R., Lu, D., Li, J., Fan, J., Zhang, Z., Liu, W. & Li, Y., 2001. An explosive seismic sounding profile across the transition zone between west Kunlun Mts. and Tarim Basin, *Sci. China Series D: Earth Sci.*, **44**, 666–672.
- Liu, S., Wang, L., Li, C., Li, H., Han, Y., Jia, C. & Wei, G., 2004. Thermal-rheological structure of lithosphere beneath the northern flank of Tarim Basin, western China: Implications for geodynamics, *Sci. China Series D: Earth Sci.*, **47**, 659–672.
- Liu, Y., Xie, H., Guo, J., Zhou, W., Xu, J.-A. & Zhao, Z., 2000. A new method for experimental determination of compressional velocities in rocks and minerals at high-pressure, *Chin. Phys. Lett.*, **17**, 924–926.
- Liu, Y., Xie, H., Zhou, W. & Guo, J., 2002. A method for experimental determination of compressional velocities in rocks and minerals at high pressure and high temperature, *J. Phys.: Condens. Matter*, **14**, 11 381–11 384.
- Lu, D., Li, Q., Gao, R., Li, Y., Li, D., Liu, W. & Zhang, Z., 2000. A deep seismic sounding profile across the Tianshan Mountains, *Chinese Sci. Bull.*, **45**, 2100–2106.
- Lu, X., He, F. & Zhao, H., 1997. The geophysical feature, structure, and evolution of the tectonic belt in the southwest margin of the Tarim Basin, *Geophys. Prospect. Petroleum*, **36**, 43–52 (in Chinese with English abstract).

- Müller, H.J., 1995. Modeling the lower crust by simulation of the in situ condition and example for the Saxonian Erzgebirge, *Phys. Earth planet. Inter.*, **92**, 3–15.
- Nover, G., 2004. Electrical properties of crustal and mantle rocks—a review of laboratory measurements and their explanation, *Surv. Geophys.*, **26**, 593–651.
- Partzsch, G.M., Schilling, F.R. & Arndt, J., 2000. The influence of partial melting on the electrical behavior of crustal rocks: laboratory examinations, model calculations and geological interpretations, *Tectonophysics*, **317**, 189–203.
- Qin, G., Chen, J., Liu, Da., Gu, Q. & Xiong, Y., 1994. The characteristics of the electrical structure of the crust and upper mantle in the region of the Kunlun and the Karakorum Mountains, *Chinese J. Geophys.*, **37**, 193–199 (in Chinese with English Abstract).
- Qiu, N., 2002. Characters of thermal conductivity and radiogenic heat production rate in Basins of northwest China, *Chinese J. Geol.*, **37**, 196–206 (in Chinese with English abstract).
- Ren, L. & Gao, Y., 2002. The role of volatiles in the formation of scapolite in amphibolites of southern West Kunlun Mountains, *Acta Petrol. Mineral.*, **21**, 398–405 (in Chinese with English Abstract).
- Roberts, J.J. & Tyburczy, J.A., 1994. Frequency dependent electrical properties of minerals and partial-melts, *Surv. Geophys.*, **15**, 239–262.
- Rudnick, R.L. & Fountain, D.M., 1995. Nature and composition of the continental crust: a lower crustal perspective, *Rev. Geophys.*, **33**, 267–309.
- Sato, H., Sacks, I.S. & Murase, T., 1989. The use of laboratory velocity data for estimating temperature and partial melt fraction in the low-velocity zone: comparison with heat flow and electrical conductivity studies, *J. geophys. Res.*, **94**, 5689–5704.
- Schilling, F.R., Partzsch, G.M., Brasse, H. & Schwarz, G., 1997. Partial melting below the magmatic arc in the central Andes deduced from geoelectromagnetic field experiments and laboratory data, *Phys. Earth planet. Inter.*, **103**, 17–31.
- Schmeling, H., 1985. Partial melt below Iceland: a combined interpretation of seismic and conductivity data, *J. geophys. Res.*, **90**, 10 105–10 116.
- Seipold, U., 1992. Depth dependence of thermal transport properties for typical crustal rocks, *Phys. Earth planet. Inter.*, **69**, 299–303.
- Shankland, T.J. & Ander, M., 1983. Electrical conductivity, temperatures, and fluids in the lower crust, *J. geophys. Res.*, **88**, 9475–9484.
- Shao, X. & Zhang, J., 1994. Preliminary results of deep structures in Tarim Basin by the method of converted waves of earthquakes, *Acta Geophys. Sin.*, **36**, 836 (in Chinese).
- Shao, X., Xu, S. & Zhou D., 1997. Structural feature of crust in Tarim Basin, *Petrol. Explor. Develop.*, **24**, 1–5 (in Chinese with English Abstract).
- Siegesmund, S., Takeshita, T. & Kern, H., 1989. Anisotropy of V_p and V_s in an amphibolite of the deeper crust and its relationship to the mineralogical, microstructural and textural characteristics of the rock, *Tectonophysics*, **157**, 25–38.
- Siegesmund, S., Vollbrecht, A. & Nover, G., 1991. Anisotropy of compressional wave velocities, complex electrical resistivity and magnetic susceptibility of mylonites from the deeper crust and their relation to the rock fabric, *Earth planet. Sci. Lett.*, **105**, 247–259.
- Simmons, G., 1964. Velocity of shear waves in rocks to 10 kbar, *J. geophys. Res.*, **69**, 1123–1130.
- Wang, D., Li, H., Yi, L., Zhang, W., Liu, C., Su, G. & Ding, D., 2002. The electrical conductivity of gabbro at high temperature and high pressure, *Chinese J. Geochem.*, **21**, 252–257.
- Wang, D., Li, H., Yi, L. & Shi, B., 2008. The electrical conductivity of upper-mantle rocks: water content in the upper mantle, *Phys. Chem. Min.*, **35**, 157–162.
- Wang, J., Wang, J.-Y., Shen, J. & Qiu, N., 1995. Heat flow in Tarim Basin, *Earth Sci.—J. China Univ. Geosci.*, **20**, 399–404. (in Chinese with English abstract).
- Wang, L., Li, C. & Yang, C., 1996. The lithospheric thermal structure beneath Tarim Basin, Western China, *Chinese J. Geophys.*, **39**, 794–803 (in Chinese with English abstract).
- Wang, Q., Ji, S., Salisbury, M., Pan, M., Xia, B. & Xu, Z., 2005a. Pressure dependence and anisotropy of P-wave velocities in ultrahigh-pressure metamorphic rocks from the Dabie-Sulu orogenic belt (China): implications for seismic properties of subducted slabs and origin of mantle reflections, *Tectonophysics*, **398**, 67–99.
- Wang, Q., Ji, S., Salisbury, M., Xia, B., Pan, M. & Xu, Z., 2005b. Shear wave properties and Poisson's ratios of ultrahigh-pressure metamorphic rocks from the Dabie-Sulu orogenic belt, China: implications for the crustal composition, *J. geophys. Res.*, **110**, doi:10.1029/2004JB003435.
- Wang, Y., Deng, J., Wang, J. & Xiong, L., 2001. Terrestrial heat flow pattern and thermo-tectonic domains in the continental area of China, *J. Graduate School Chinese Acad. Sci.*, **18**, 51–58 (in Chinese with English abstract).
- Xiao, W., Windley, B.F., Chen, H., Zhang, G. & Li, J., 2002. Carboniferous–Triassic subduction and accretion in the western Kunlun, China: implications for the collisional and accretionary tectonics of the northern Tibetan plateau, *Geology*, **30**, 295–298.
- Xie, H., Zhang, Y., Xu, H. G., Hou, W., Guo, J. & Zhao, H., 1993. A new method of measurement for elastic wave velocities in minerals and rocks at high temperature and high pressure and its significance, *Sci. China, Ser. B*, **36**, 1276–1280.
- Xu, J., Zhang, Y., Hou, W. *et al.*, 1994. Measurements of ultrasonic wave velocities at high temperature and high pressure for window glass, pyrophyllite, and kimberlite up to 1400°C and 5.5 GPa, *High Temp.-High Pressure*, **26**, 375–384.
- Xu, Y.-S., Poe, B., Shankland, T.J. & Rubie D.C., 1998. Electrical conductivity of Olivine, wadsleyite, and ringwoodite under upper-mantle conditions, *Science*, **280**, 1415–1418.
- Zhang, J., Shao, X. & Fan, H., 1998. Deep sounding survey by converted waves of earthquakes in center part of the Tarim Basin and its interpretation, *Seismol. Geol.*, **20**, 34–36 (in Chinese with English abstract).
- Zhang, X., Zhao, J., Zhang, C., Ren, Q., Nie, W., Cheng, S., Pan, S. & Tang, Z., 2002. Crustal structure at the northeast side of the Pamirs, *Chinese J. Geophys.*, **45**, 665–671.
- Zhao, Y., Lawson, A.C., Zhang, J., Bennett, B.I. & von Dreele, R.B., 2000. Thermoelastic equation of state of molybdenum, *Phys. Rev. B*, **62**, 8766–8776.
- Zhao, Z., Xie, H., Zhou, W., Christensen, N.I. & Zhang, Z., 2001. Elastic wave velocity in rocks from Dabieshan and its constraints for the lithospheric composition and crust-mantle recycling, *Prog. Natural Sci.*, **11**, 115–112.
- Zhu, M., Xie, H., Guo, J., Bai, W. & Xu, Z., 2001. Impedance spectroscopy analysis on electrical properties of serpentine at high pressure and high temperature, *Sci. China, Ser. D*, **44**, 336–345.